 CMES, vol.2, no.2, pp.155-170, 2001

Three-dimensional Numerical Simulation of Unsteady Marangoni Convection in the CZ Method using GSMAC-FEM

Haruhiko Kohno, Takahiko Tanahashi[1]

Abstract: Three-dimensional (3D) unsteady numerical simulations are carried out by means of the finite element method (FEM) with the generalized simplified marker and cell (GSMAC) method in silicon melt with a non-deformable free surface with Prandtl number Pr = 1.8534×10^{-2}, Marangoni number Ma = $0.0 - 6.2067 \times 10^2$, Grashof number Gr = 7.1104×10^6, and the aspect ratio As = 1.0 in the Czochralski (CZ) method. The flow state becomes unstable earlier by increasing the absolute value of the thermal coefficient of surface tension in the range of $\sigma_T = 0.0 - 1.5 \times 10^{-5}$N/mK. Although the velocity distribution in the circumferential direction is isotropy in any direction first, its magnitude becomes periodic and has the wavelength equal to 1/8 of the circumference. Then the wavelength doubles, and the flow pattern becomes finally asymmetrical. Moreover, the oscillation of the velocity distribution is observed just under the single crystal, and the amplitude is found to depend on the value of σ_T. After imposing the vertical magnetic field more than 0.05T to the melt from 50s, the flow pattern becomes restored to symmetry. But the instability remains under the single crystal and it indicates that the influence of Marangoni convection can not be neglected in the crystal growing process.

keyword: Marangoni convection, Czochralski method vertical magnetic field, GSMAC-FEM

1 Introduction

CZ method is a widely adopted crystal growth technique whose product is superior in mechanical strength and is becoming a promising technique to realize large caliber single crystals of semiconductors from the melt. The product is manly used as an integrated circuit which is in a television, a video, a machine for measurement or control and so on. For the coming information society, the importance of the material base is acquiring.

It is well known that three kinds of convection: the compulsory convection, the natural convection, and Marangoni convection [Schwabe and Scharmann (1979); Sumiji, Nakamura, Omura, and Hibiya (2000)] are generated in fluid in the CZ process. It is necessary for the production of good quality single crystal that the flow is well stirred with the structure kept axisymmetrical and moderate near the interface between a single crystal and melt by controlling these kinds of convection. The compulsory convection occurs by the external force when the crucible or the grown single crystal rotates constantly. The natural convection in fluid and Marangoni convection on the free surface are both generated when the gradient of temperature exists at each place. The former is driven by the buoyancy and the latter is done by the gradient of surface tension. Although Marangoni convection is observed remarkably under microgravity, its behavior is usually hidden in fluid under normal gravity because of the influence of the natural convection. Some experiments and numerical simulations dealing with Marangoni convection under microgravity have been done so far [Nakamura, Hibiya, Kakimoto, Imaishi, Nishizawa, Hirata, Mukai, Yoda, and Morita (1998); Imaishi, Yasuhiro, Sato, and Yoda (1999); Zeng, Mizuseki, Higashino, and Kawazoe (1999)]. The magnitude of surface tension depends on temperature, concentration, and electric potential, and it is difficult to investigate the effect of each element to the surface tension separately and get reliable experimental data. This is one reason why the effects of Marangoni convection have rarely described in the CZ method even today. Some CZ process experiments are performed with the oxidized contamination left on the free surface intentionally to remove the effects of Marangoni convection [Lee and Chun (1997)]. But in the real process, the effect of the surface tension is essential because the temperature difference and the partial difference of the oxygen concentration on

[1] Keio University, 3-14-1, Hiyoshi, Kohoku-ku, Yokohama, 223-8522 JAPAN, E-mail: kohno@tana.mech.keio.ac.jp; taka@mech.keio.ac.jp

the free surface can not be neglected [Azami, Nakamura, Hibiya, and Mukai (2000)]. So it is important to introduce Marangoni convection into the numerical simulation to make a precise analysis of the CZ method even if some approximations are needed for that.

In the present study, we perform a series of three-dimensional numerical simulations with the parameter of Marangoni convection changed within a small range in adiabatic silicon melt with flat free surface. Surface tension is assumed to depend on only temperature, and so the effect of concentration is not taken into consideration. Moreover, the vertical magnetic field is imposed after 50s, and the comparison between Marangoni convection and a slip condition is made after that. However, in this paper, discussions are restricted to the state with the single crystal and the crucible static. The rotational effects of them will be reported in another forthcoming paper. The purpose of this paper is to clarify the influence which Marangoni convection gives to the flow structure and the interface between a single crystal and melt, and the behavior that the effects will be damped by imposing the vertical magnetic field.

2 List of symbols

$\mathbf{B}_0$	applied magnetic flux density
C_p	specific heat
D	rate of strain tensor
$\mathbf{g}$	gravitational acceleration
$\mathbf{I}$	unit tensor
$\mathbf{J}$	current density
$\mathbf{n}$	unit normal vector
p	pressure
$\mathbf{s}$	unit vector which points to the direction of the surface tension
t	time
$\mathbf{t}_1, \mathbf{t}_2$	unit vectors on the tangential plane, which cross with the normal vector vertically on the free surface
$\mathbf{t}^{(n)}$	stress vector
$\mathbf{t}_\sigma$	surface tension vector
$\mathbf{T}$	temperature
$\mathbf{T}$	stress tensor
$\mathbf{v}$	velocity
α	thermal diffusivity
β	coefficient of cubical expansion
ϕ	scalar potential
μ	coefficient of viscosity
ν	kinematic viscosity
ρ	density
σ	surface tension
σ_m	electric conductivity
σ_T	thermal coefficient of surface tension
$\Sigma, \partial\Sigma$	closed area and closed curve, respectively
$\nabla_\perp, \nabla_{//}$	normal component and tangential plane component of the nabla operator, respectively

3 The theory of surface tension

The surface tension vector is defined in the following equation:

$$t_\sigma = \lim_{\Sigma\to 0} \frac{1}{\Sigma} \oint_{\partial\Sigma} \sigma \mathbf{s} dl \tag{1}$$

With the surface divergence theorem, the surface tension vector is described as follows:

$$t_\sigma = \nabla_{//}\sigma - \sigma\left(\nabla_{//}\cdot\mathbf{n}\right)\mathbf{n} \tag{2}$$

The equation (2) can be proved by the surface divergence theorem. First of all, we describe the surface nabla operator.

Step 1: The nabla operator is resolved into the normal component and the tangential plane component which are described in the following equations:

$$\nabla = \nabla_\perp + \nabla_{//} \tag{3}$$

$$\nabla_\perp = \mathbf{n}\left(\mathbf{n}\cdot\nabla\right) \tag{4}$$

$$\nabla_{//} = \mathbf{t}_1\left(\mathbf{t}_1\cdot\nabla\right) + \mathbf{t}_2\left(\mathbf{t}_2\cdot\nabla\right) \tag{5}$$

Step 2: Second, we prove the surface divergence theorem with the surface nabla operator. The round integral which goes around the closed curve $\partial\Sigma$is changed by the Stokes' theorem into the following equation:

$$\oint_{\partial\Sigma} \sigma\mathbf{s}dl = \oint_{\partial\Sigma} d\mathbf{l}\times\sigma\mathbf{n} = \int_\Sigma (\mathbf{n}\times\nabla)\times\sigma\mathbf{n}d\Sigma \tag{6}$$

$$(\mathbf{n}\times\nabla)\times\sigma\mathbf{n} = \sigma\{(\mathbf{n}\times\nabla)\times\mathbf{n}\} + \{\mathbf{n}\times(\nabla\sigma)\}\times\mathbf{n} \tag{7}$$

Substitution of the equations (3) , (4), and (5) into the equation (7) leads the following equation:

$$(\mathbf{n}\times\nabla)\times\sigma\mathbf{n} = \nabla_{//}\sigma - \sigma\mathbf{n}\left(\nabla_{//}\cdot\mathbf{n}\right) \tag{8}$$

Thus, the equation (2) is obtained by substituting the equation (6) and (8) into the equation (1).

$$\begin{aligned}\mathbf{t}_\sigma &= \lim_{\Sigma\to 0}\frac{1}{\Sigma}\int_\Sigma \{\nabla_{//}\sigma - \sigma\mathbf{n}\left(\nabla_{//}\cdot\mathbf{n}\right)\}d\Sigma \\ &= \nabla_{//}\sigma - \sigma\mathbf{n}\left(\nabla_{//}\cdot\mathbf{n}\right)\end{aligned} \tag{9}$$

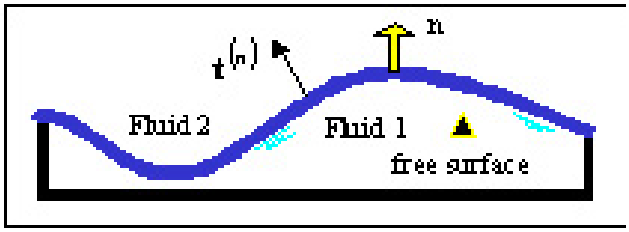

Figure 1 : Two-phase model

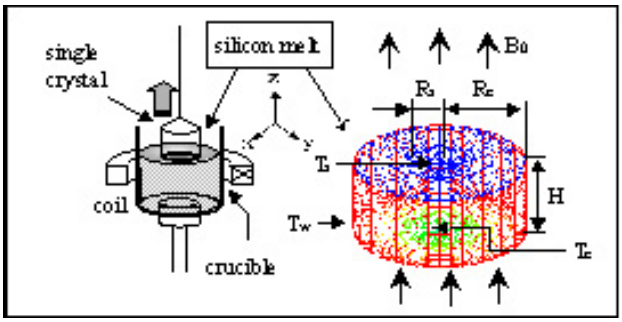

Figure 2 : Mathematical model in the CZ method.

The surface tension vector is included in the equation of the boundary condition which causes Marangoni convection. Fig.1 shows a two-phase model which is divided into two areas: Fluid 1 and Fluid 2, by the free surface. In this study the calculation is conducted only in the area of Fluid 1. The boundary condition of the free surface is given by the following equation:

$$\left[\mathbf{t}^{(n)}\right]_2^1 = \mathbf{t}_\sigma = \nabla_{//}\sigma - \sigma\left(\nabla_{//}\cdot\mathbf{n}\right)\mathbf{n} \tag{10}$$

The equation (10) means that the jump of the stress vector on the free surface is equal to the surface tension vector. The stress vector is described as follows by the Cauchy's basic law:

$$\mathbf{t}^{(n)} = \mathbf{n}\cdot\mathbf{T} \tag{11}$$

Besides, the stress tensor is expressed in the following constitutive equation by the Navier-Poisson's law in terms of the incompressible fluid:

$$\mathbf{T} = -p\mathbf{I} + 2\mu\mathbf{D} \tag{12}$$

Then the following equation is obtained by substituting the equation (11), (12) into the equation (10).

$$[\mathbf{n}\cdot(-p\mathbf{I}+2\mu\mathbf{D})]_2^1 = \nabla_{//}\sigma - \sigma\left(\nabla_{//}\cdot\mathbf{n}\right)\mathbf{n} \tag{13}$$

The left-hand term in the equation (13) can be expanded with the attached letter notation as follows:

$$\begin{aligned}&\left[-pn_i+\mu\left(\frac{\partial u_j}{\partial x_i}+\frac{\partial u_i}{\partial x_j}\right)n_j\right]_2^1\\ &= -p_l n_i = \mu_i\left(\frac{\partial u_j}{\partial x_i}+\frac{\partial u_i}{\partial u_j}\right)_1 n_j\\ &= -pn_i+\mu\frac{\partial u_j}{\partial x_i}n_j+\mu\frac{\partial u_i}{\partial n}\end{aligned} \tag{14}$$

Here the pressure and the velocity in Fluid 2 are both assumed to be 0. The first term on the right-hand side in the equation (13) can be changed into the following form by applying the chain rule.

$$\nabla_{//}\sigma = \left(\frac{\partial\sigma}{\partial T}\right)\nabla_{//}T \tag{15}$$

Here the thermal coefficient of surface tension σ_T is defined in the following equation:

$$\sigma_T = \frac{\partial\sigma}{\partial T} \tag{16}$$

Moreover, the second term on the right-hand side in the equation (13) can be omitted by the postulate in which the free surface is flat and non-deformable. Therefore the following equation is lead by substituting the equation (14), (15), and (16) into the equation (13).

$$pn_i - \mu\frac{\partial u_i}{\partial n} = -\sigma_T\nabla_{//}T + \mu\frac{\partial u_j}{\partial x_i}n_j \tag{17}$$

After taking the surface integral of the equation (17), the second term on the right-hand side is eliminated by applying the Gauss' theorem in terms of the incompressible fluid.

$$\iint_\Gamma\left(pn_i - \mu\frac{\partial u_i}{\partial n}\right)d\Gamma = -\iint_\Gamma\sigma_T\nabla_{//}T\,d\Gamma \tag{18}$$

The equation (18) is called a boundary integral term and adopted as an equation which gives a boundary condition of the FEM.

4 Mathematical model

A schematic diagram and a mathematical model of the silicon melt in the CZ method are shown in Fig.2.

The melt depth and the crucible radius are divided into 26 and 29 elements each, and the whole node and element numbers are 38259 and 36192, respectively. The

Table 1 : Size of crucible and boundary condition parameters

Crucible Radius	[m]	R_c	2.50×10^{-2}
Crystal Radius	[m]	R_s	8.97×10^{-3}
Melt Depth	[m]	H	2.50×10^{-2}
Crystal / Melt Interface Temp.	[K]	T_s	1685.0
Crucible Wall Temp.	[K]	T_w	1745.0
Central Temp. at the Bottom	[K]	T_c	1705.0
Magnetic Flux Density	[T]	B_0	0.01 - 0.1

Table 2 : Physical properties of silicon melt

Melt Density	[kg/m^3]	ρ	2.33×10^3
Kinematic Viscosity	[m^2/s]	ν	4.30×10^{-7}
Thermal Coeff. of Surface Tension	[N/mK]	σ_T	$-1.00 \times 10^{-5} - 0.00$
Thermal Diffusivity	[m^2/s]	α	2.32×10^{-5}
Electric Conductivity	[S/m]	σ_m	1.06×10^6
Specific Heat	[J/kgK]	C_p	1.00×10^3
Coefficient of Cubical Expansion	[l/K]	β	1.43×10^{-4}

hexahedron elements are used, and the elements near the boundary layer are divided smaller in order to make an accurate calculation. The liquid with a flat free surface maintains a cylindrical shape and the temperature of the side wall, the bottom wall, and the interface between the crystal and the melt are constant. The slope of the temperature is constant linearly from the side (T_w) to the center (T_c) at the bottom wall. The thermophysical properties of the silicon melt are assumed to be constant except for the thermal coefficient of surface tension σ_T. The top liquid surface is assumed to be adiabatic. This approximation is grounded on the fact that the temperature of the inert gas around the crucible is close to the one of the melt.

At the initial stage, the liquid is at rest with the constant temperature T_s. At t = 0s, the temperature of the side wall and the bottom wall is instantaneously raised and kept at $T_w$and T_c while the interface between the crystal and the melt is maintained at T_s. The computation has been done by using the Cartesian coordinates system with a non-uniform grid.

A set of boundary condition parameters and physical properties of silicon melt are listed in Tab. 1 and Tab. 2.

5 The governing equations

The governing equations in the velocity, temperature, and magnetic fields are described with boundary conditions as follows:

Continuity equation :

$$\nabla \cdot \mathbf{v} = 0 \tag{19}$$

Navier-Stokes equation:

$$\rho \left(\frac{\partial \mathbf{v}}{\partial t} + \mathbf{v} \cdot \nabla \mathbf{v} \right) = -\nabla p + \mu \nabla^2 \mathbf{v} - \rho \beta \mathbf{g} (T - T_s) + \mathbf{J} \times \mathbf{B}_0 \tag{20}$$

Energy equation:

$$\frac{\partial T}{\partial t} + \mathbf{v} \cdot \nabla T = \alpha \nabla^2 T + \frac{1}{\rho \sigma_m C_p} \mathbf{J}^2 \tag{21}$$

Ohm's law:

$$\mathbf{J} = \sigma_m (-\nabla \phi + \mathbf{v} \times \mathbf{B}_0) \tag{22}$$

Principle of conservation of charge:

$$\nabla \cdot \mathbf{J} = 0 \tag{23}$$

Boundary conditions:

$$\begin{array}{lll} \underline{\text{at r = R}_c} & & \mathbf{v}=0, T=T_w \\ \underline{\text{at z = 0}} & & \mathbf{v}=0, T=T_c-T_w \\ \underline{\text{at z = H}} & & \\ & 0\le r\le R_s & \mathbf{v}=0, T=T_s \\ & R_s<r<R_c & pn_i-\mu\dfrac{\partial u_i}{\partial n}=-\sigma_T\nabla_{//}T \\ & & +\mu\dfrac{\partial u_j}{\partial x_i}n_j(\text{free surface}) \end{array} \tag{24}$$

"r" stands for the distance from the center axis in the equation (24). The Boussinesq approximation is applied in the equation (20) on the ground that the temperature difference between the crucible and the crystal is not so large. The non-dimensional parameters are defined with the following scaling lists: an aspect ratio As = H/R_c, Prandtl number Pr = ν/α, Marangoni number Ma = $|\sigma_T|\Delta T H/(\rho\nu\alpha)$, Grashof number Gr = $\beta\Delta T g H^3/\nu^2$.

6 Numerical method

The governing equations with the boundary conditions are solved by the FEM with the GSMAC method [Tanahashi, Okanaga, and Saito (1990); Tanahashi, Oki, and Henjes (1993)]. The GSMAC method is an application of the HSMAC scheme to the finite element method, so the numerical procedure is based on the projection method in which the fields of pressure and velocity are obtained by solving the Poisson's equation simultaneously. GSMAC-FEM satisfies three important elements of calculation: accuracy, universality, and economy.

First the time marching method is adopted in which the Navier-Stokes equation (20) is discretized explicitly on the velocity **v** and implicitly on the pressure p.

$$\frac{\mathbf{v}^{n+1}-\mathbf{v}^n}{\Delta t}=-\frac{1}{\rho}\nabla p^{n+1}-(\mathbf{v}^n\cdot\nabla)\,v^n+\nu\nabla^2\mathbf{v}^n - \beta\mathbf{g}(T^n-T_s)+\frac{1}{\rho}\mathbf{J}^n\times\mathbf{B}_0^n \tag{25}$$

The pressure $p^{n+1}$is separated into two parts by using the correcting value p^c.

$$p^{n+1}=p^n+p^c \tag{26}$$

Then the equation (25) is separated into two parts of the equations (27) and (28) by using the predictor velocity $\tilde{v}$.

$$\frac{\tilde{\mathbf{v}}-\mathbf{v}^n}{\Delta t}=-\frac{1}{\rho}\nabla p^n-(\mathbf{v}^n\cdot\nabla)\,\mathbf{v}^n+\nu\nabla^2\mathbf{v}^n - \beta\mathbf{g}(T^n-T_s)+\frac{1}{\rho}\mathbf{J}^n\times\mathbf{B}_0^n \tag{27}$$

$$\frac{\mathbf{v}^{n+1}-\tilde{\mathbf{v}}}{\Delta t}=-\frac{1}{\rho}\nabla p^c \tag{28}$$

The continuity equation is true at all times as far as fluid keeps incompressible. Thus the equation (19) can be discretized as follows with the next time step n+1:

$$\nabla\cdot\mathbf{v}^{n+1}=0 \tag{29}$$

Taking the divergence of the equation (28) considering the equation (29), the following equation is obtained.

$$\nabla\cdot\frac{\tilde{\mathbf{v}}}{\Delta t}=\frac{1}{\rho}\nabla^2 p^c \tag{30}$$

The equation (30) is the Poisson's equation in terms of velocity and pressure. To solve these physical quantities simultaneously, the correcting velocity potential ϕ_p is defined in the following equation:

$$\phi_p=p^c\Delta t \tag{31}$$

Then the equation (30) and the next time step values of velocity and pressure are expressed in the following forms by using ϕ_p, respectively:

$$\frac{1}{\rho}\nabla^2\phi_p=\nabla\cdot\tilde{\mathbf{v}} \tag{32}$$

$$p^{n+1}=p^n+\frac{\phi_p}{\Delta t} \tag{33}$$

$$\mathbf{v}^{n+1}=\tilde{\mathbf{v}}-\frac{1}{\rho}\nabla\phi_p \tag{34}$$

The computation of the equations (32) - (34) is iterated until the value on the left-hand side of the equation (29) is below the criterion 1.0×10^{-3} in the computational space. The max iteration number is set 1000 in this study.

Second the equation (22) of the Ohm's law is discretized explicitly on the velocity **v** and implicitly on the scalar potential ϕ.

$$\mathbf{J}^{n+1}=\sigma_m\left(-\nabla\phi^{n+1}+\mathbf{v}^{n+1}\times\mathbf{B}_0\right) \tag{35}$$

The calculation of the equation (35) is conducted after solving the velocity field. Thus the velocity vector $\mathbf{v}^{n+1}$

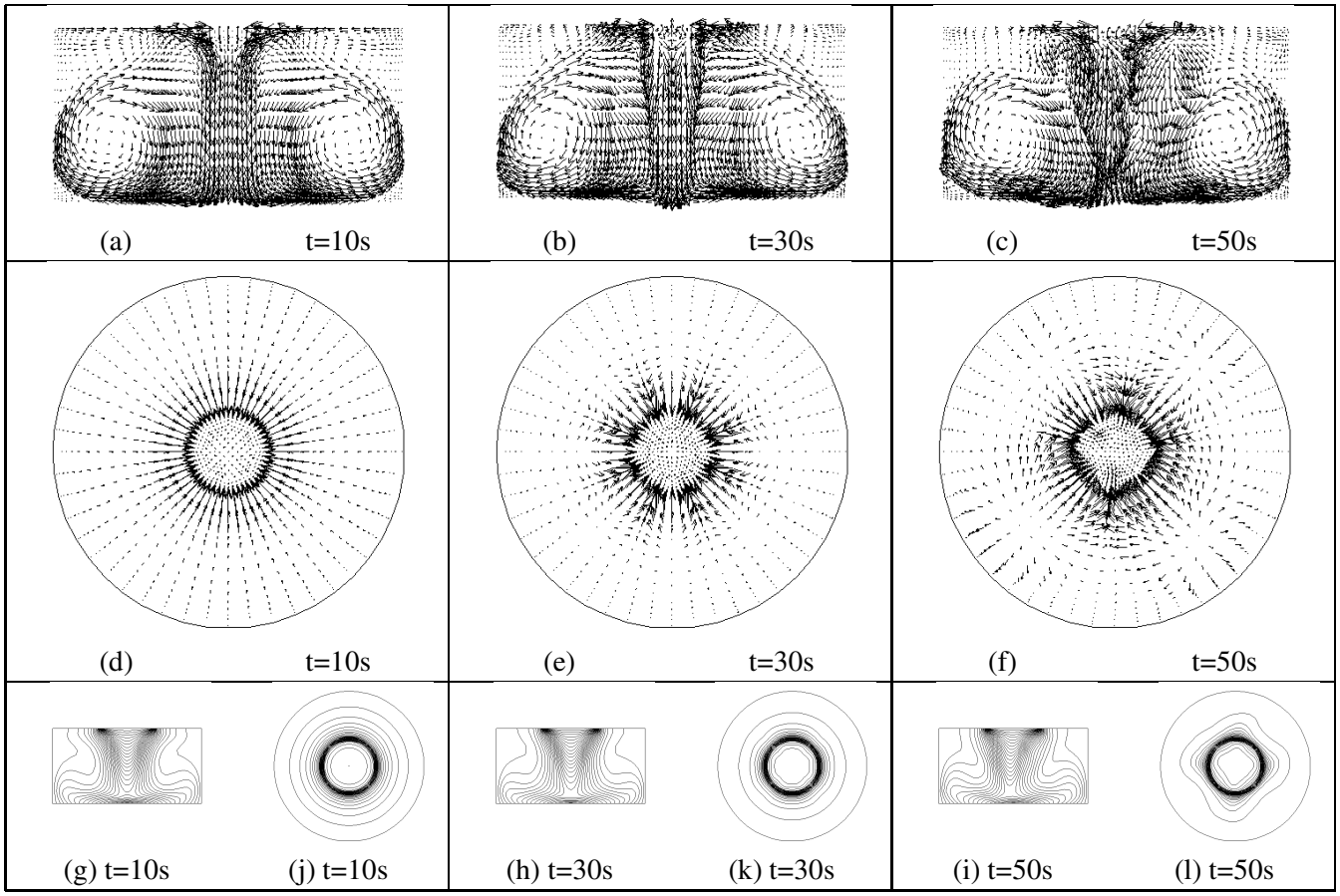

Figure 3 : Projected velocity and contour lines of temperature on the vertical plane (a) - (c) and (g) - (i), respectively at y=0.00m and the horizontal cut (d) - (f) and (j) - (l) at z=2.47×10^{-2} with $\sigma_T = -1.0 \times 10^{-5}$N/mK.

has already been obtained by this time. The scalar potential ϕ^{n+1} is separated into two parts by using the correcting value ϕ^c.

$$\phi^{n+1} = \phi^n + \phi^c \tag{36}$$

Then the equation (35) is separated into two parts of the equation (37) and (38) by using the predictor current density $\tilde{\mathbf{J}}$.

$$\mathbf{J}^{n+1} = \tilde{\mathbf{J}} - \sigma_m \nabla \phi^c \tag{37}$$

$$\tilde{\mathbf{J}} = \sigma_m \left(-\nabla \phi^n + \mathbf{v}^{n+1} \times \mathbf{B}_0 \right) \tag{38}$$

The principle of conservation of charge is always true just like the continuity equation in the velocity field. Thus the equation (23) can be discretized as follows with the next time step n+1:

$$\nabla \cdot \mathbf{J}^{n+1} = 0 \tag{39}$$

The divergence of the equation (37) in the help of the equation (39) leads to the following Poisson equation again:

$$\sigma_m \nabla^2 \phi^c = \nabla \cdot \tilde{\mathbf{J}} \tag{40}$$

The next time step values of current density and scalar potential are obtained by the iteration of the equations (36), (37), and (40). This process is continued until the value of the left-hand side of the equation (39) is below the criterion 1.0×10^{-2} in the computational space. The max iteration number is set 500 in this study.

Third the energy equation (21) is discretized explicitly as follows:

$$\frac{T^{n+1} - T^n}{\Delta t} = -\left(\mathbf{v}^{n+1} \cdot \nabla\right) T^n + \alpha \nabla^2 T^n + \frac{1}{\rho \sigma_m C_p} \left(\mathbf{J}^{n+1}\right)^2 \tag{41}$$

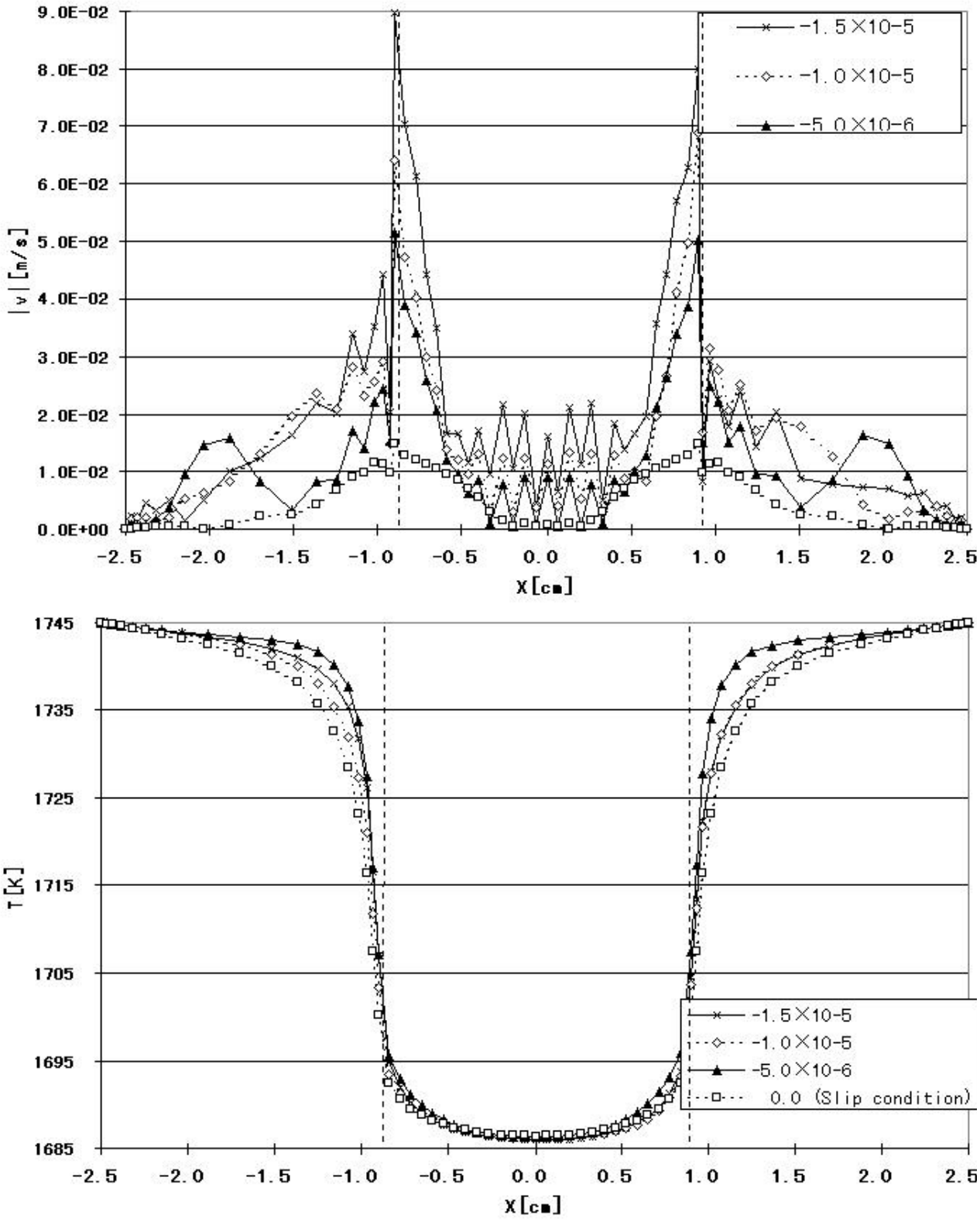

Figure 4 : Velocity and temperature distribuations near the interface with the parameter σ_T at y = 0.00m and z=2.47×10^{-2}m.

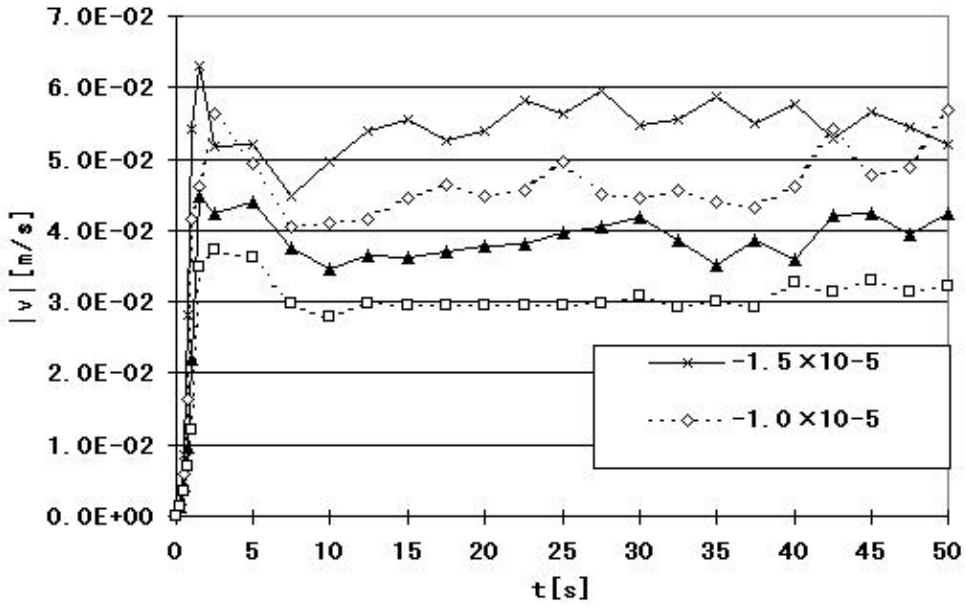

Figure 5 : Time Evolution of velocity with the parameter σ_T at r = 0.00m and z = 1.25×10^{-2}m.

The next time step value of temperature is thus obtained by solving the equation (41) directly.

The time step width Δt is chosen 5×10^{-4}s, and the computation is done until 70s.

7 Results

A comparison with experimental results is carried out to check the validation of this code. In this case, a liquid bridge with Ma = 28275, Pr = 7, and Gr = 240.95 is adopted as a mathematical model. The periodic oscillatory frequency f = 1.594 1/s is obtained, which is comparable with f = 1.357 1/s (way up) and f = 1.318 1/s (way down) [Frank and Schwabe (1997)]. This value is also close to other numerical result f = 1.226 1/s on the same condition [Zeng, Mizuseki, Higashino, and Kawazoe (1999)].

The magnitude of surface tension depends on temperature. When the temperature is high on part of free surface, the surface tension becomes small. But if the temperature is low, the surface tension becomes large. Thus the magnitude of surface tension is small near the crucible and large near the interface between the single crystal and the melt in this study, and it causes the surface tension driven flow.

The flow structures with $\sigma_T = -1.0 \times 10^{-5}$ N/mK show axisymmetry on the vertical plane at 10s and 30s in Fig. 3 (a), (b). However, the structures are different at each time in terms of the horizontal cut near the free surface. Although the velocity distribution is isotropy at 10s in Fig.3 (d), it becomes symmetrical at 30s and has 8 modes (see Fig. 3 (e)). Moreover, at 50s, the axisymmetrical structure is lost on the vertical plane (see Fig. 3 (c)). At this stage, the velocity vectors point to the azimuthal direction near the center of the radius on the horizontal cut and the mode number decreases to 4 as shown in Fig. 3 (f). These behaviors of the velocity field are reflected in contour lines of temperature in Fig. (g) - (l). Although Fig. 3 (g) and (h) show the axisymmetrical structure, the pattern becomes asymmetrical at 50s as shown in Fig. 3 (i). On the horizontal cut, the shape of contour lines is a complete circle at 10s in Fig.3 (j). But it changes into 8-fold symmetrical structure at 30s, and finally 4-fold asymmetrical one as shown in Fig. 3 (k), (l).

The magnitude of velocity goes down largely under the interface between the single crystal and the melt at any σ_T as shown in Fig. 4 (a). When σ_T is 0.0N/mK, i.e. the slip condition is applied, the magnitude of the velocity is relatively small and stable. But as the absolute value of the coefficient increases, the oscillation of velocity under the interface is observed and its amplitude also grows larger. This oscillatory behavior is considered a kind of instability generated by the crash of the flow with high velocity and the postulate of the non-slip condition

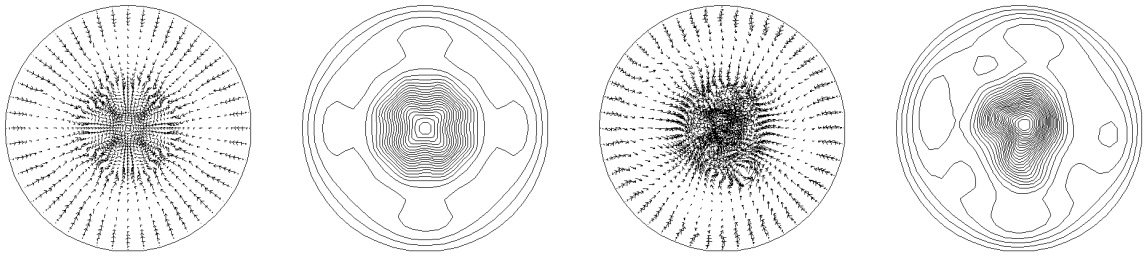

(a) t=50s (b) t=50s (c) t=50s (d) t=50s

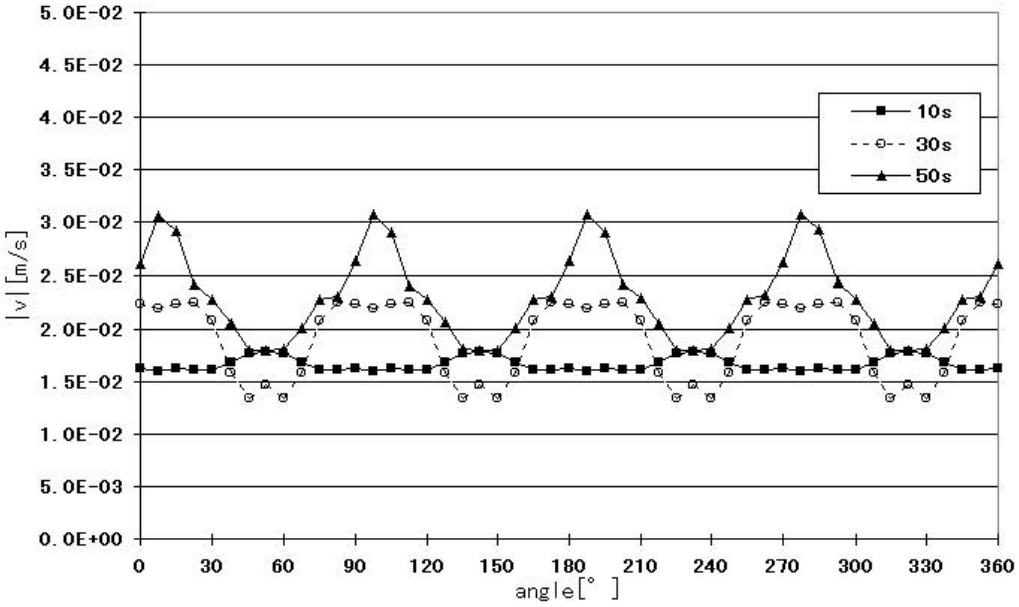

(e)

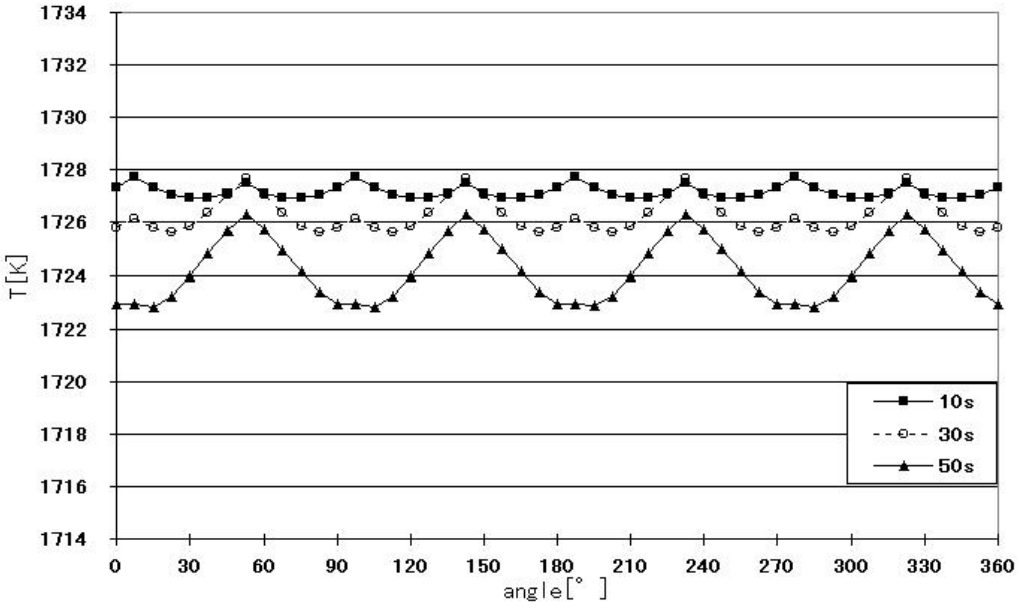

(f)

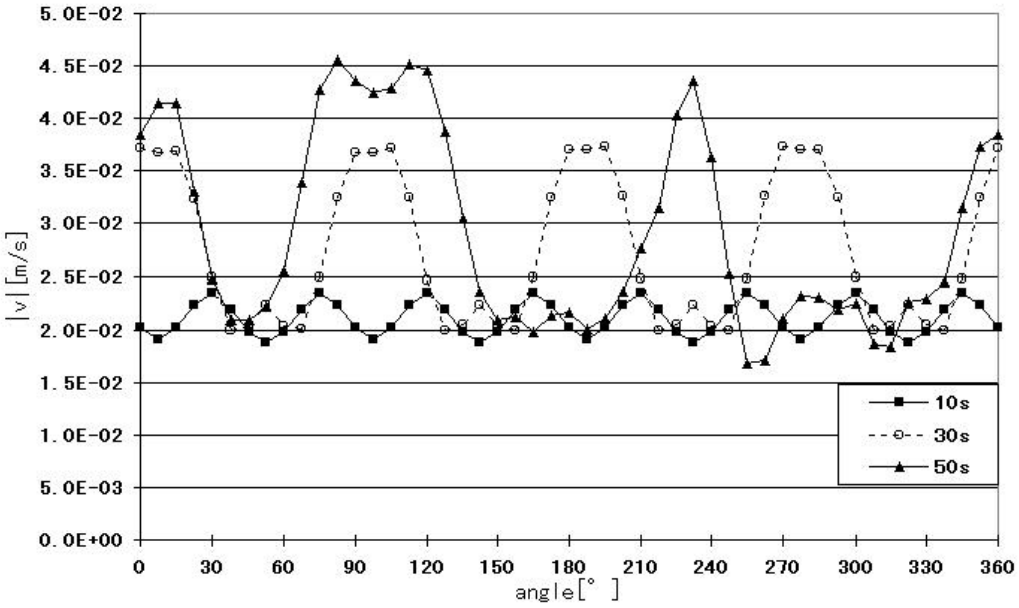

(g)

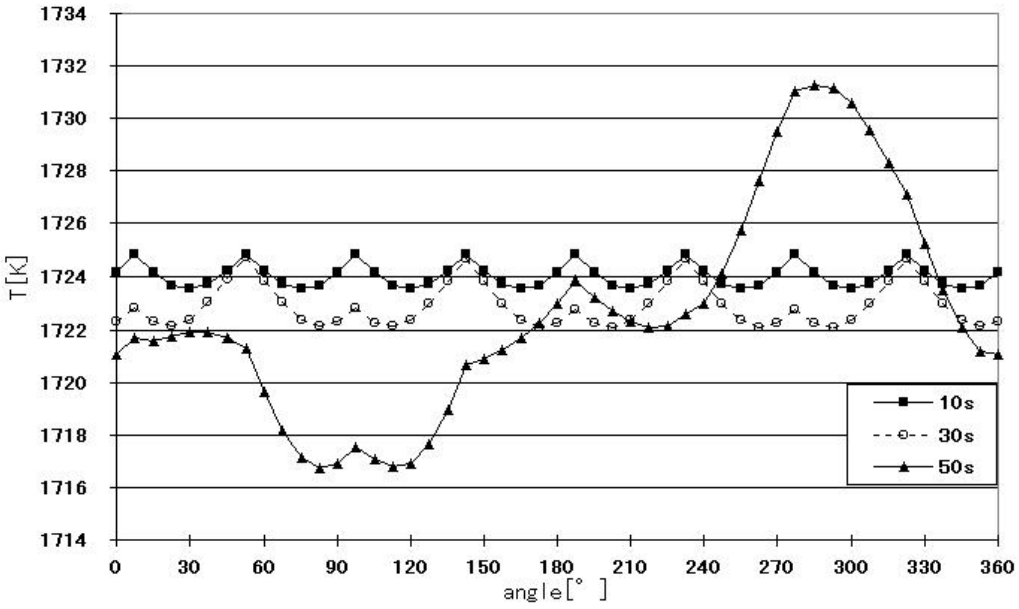

(h)

Figure 6 : Comparison of prjected velocity and contour lines of temperature between a slip condition(a),(b) and Marangoni convection (c),(d) with $\sigma_T = -1.0 \times 10^{-5}$m and their circumferential distributions between a slip condition (e), (f) and Marangoni covection (g), (h) at $r = 4.62 \times 10^{-3}$m, z=1.25×10^{-2}.

on the solid-melt interface. Of course, this phenomenon will have a harmful effect on good quality single crystal because of the lack of material uniformity. The reason why the magnitude of velocity drastically goes up near the brim of the single crystal is that the flow is accelerated by the large gradient of surface tension. Although high temperature is traveled from the crucible to the center of the melt on the free surface by the convection, the temperature of the single crystal is kept T_s. So the local and steep gradient of the surface tension is caused by this large difference of temperature.

In comparison with the velocity field, the difference of the distributions depending on σ_T under the interface is not so clear in the temperature field as shown in Fig. 4 (b). Moreover, the oscillatory behavior is not observed so clearly and the distributions are relatively smooth. The largest gradient near the brim of the single crystal is confirmed in $\sigma_T = -5.0 \times 10^{-6}$ N/m in this study.

Fig.5 shows the time evolution of the magnitude of velocity with the parameter σ_T at the center of the melt. The reason why the magnitude of velocity greatly increases at each condition within 5s is that the melt is quiescent at 0s and the driving forces of the natural convection and Marangoni convection are the maximum at this stage because the temperature difference between the melt and the crucible is the maximum at the initial condition. In this study the direction of the natural convection and Marangoni convection is the same near the free surface. So the generation of Marangoni convection encourages the natural convection, and the magnitude of velocity becomes larger as the increase of the absolute value of σ_T as proved in the equation (24). Fig. 5 also shows that there is an oscillation of the magnitude of the velocity at the center of the melt in each σ_T after the constant increase. This oscillatory behavior means the instability of the flow condition and occurs earlier as the increase of the absolute value of σ_T.

Fig. 6 shows the comparison of velocity and temperature distributions between a slip condition and Marangoni convection at the central height of the melt. On a slip condition, 4 symmetrical modes are observed in both velocity and temperature fields at 50s (see Fig. 6 (a), (b)). This is also confirmed from the circumferential distributions as shown in Fig. 6 (e), (f). The wavelengths of the magnitude of velocity and temperature correspond to 1/4 and 1/8 of the circumference respectively at 10s, and the amplitudes become larger as time passes. Finally, the

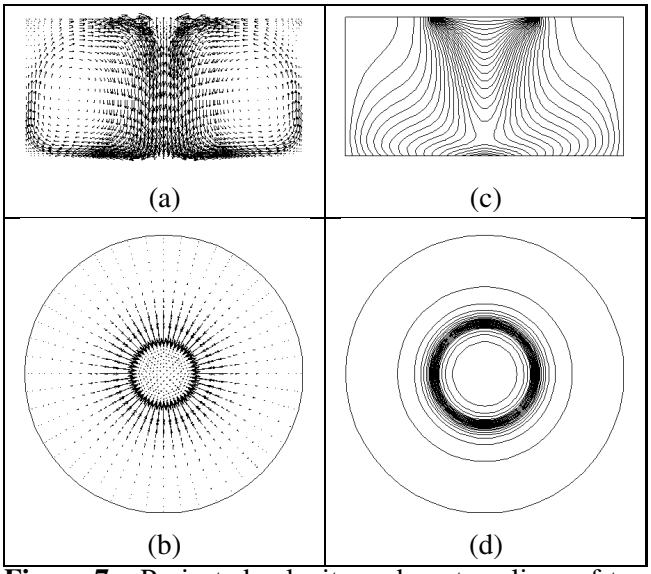

Figure 7 : Projected velocity and contour lines of temperature with $\sigma_T = -1.0 \times 10^{-5}$N/mK, B_0 = 0.05T on a vertical plane (a), (c) at y =0.00 and a horizontal cut (b), (d) at z = 2.47×10^{-2}m, respectively.

wavelengths of both velocity and temperature fields become 1/4 of the circumference at 50s. There are two reasons why the temperature goes down with time in Fig. 6 (f). First, both temperature and surface tension gradients become smaller by the decrease of temperature difference. This brings about a decline of the convection intensity related with the magnitude of the buoyancy and the Marangoni effect. Second, the effect of the cold temperature area is transformed gradually to the central height of the melt. However, in the case considering the effect of Marangoni convection, it is found that the flow pattern becomes asymmetrical at 50s in Fig. 6 (c), (d). In Fig. 6 (g), (h), the wavelengths of the magnitude of both velocity and temperature are equal to 1/8 of the circumference at 10s. Then the wavelengths double in each field at 30s, and finally the periodic nature is destroyed at 50s. In Fig. 6 (h), it is observed that the temperature distribution is divided into two areas, i.e. low and high areas at 50s, and the difference between two areas is much larger than the amplitude of 10s or 30s. These phenomena show the onset of turbulent flow.

Fig. 7 shows the velocity and temperature distributions considering the effect of Marangoni convection at 70s with the vertical magnetic field B_0 = 0.05T. By imposing the vertical magnetic field, the Lorentz force is generated in the opposite direction of the flow at the top and bottom

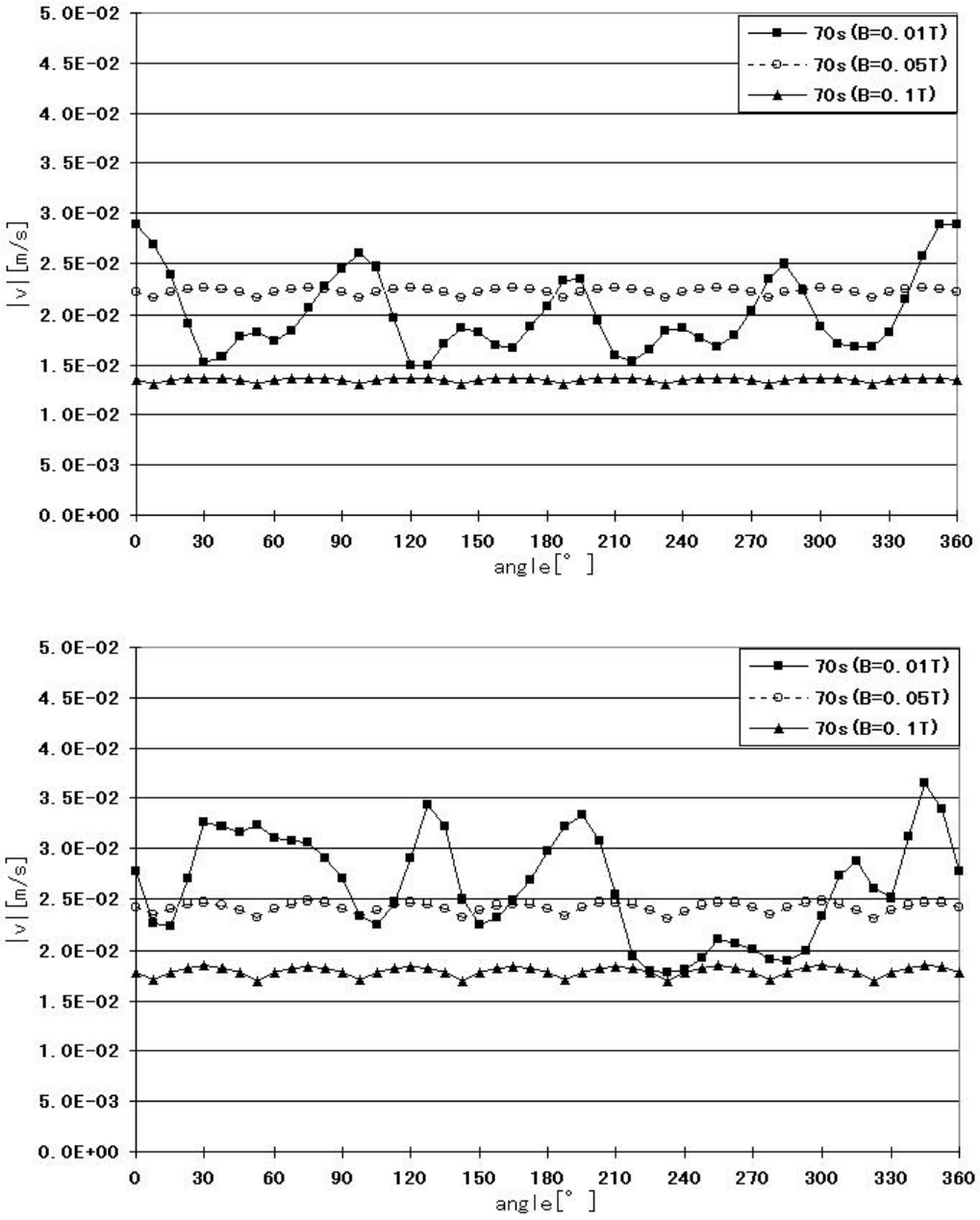

Figure 8 : Comparison of the circumferential velocity distributions between a slip condition (a) and (b) at $r = 4.62 \times 10^{-3}$m, $z = 1.25 \times 10^{-2}$m with the parameter B_0.

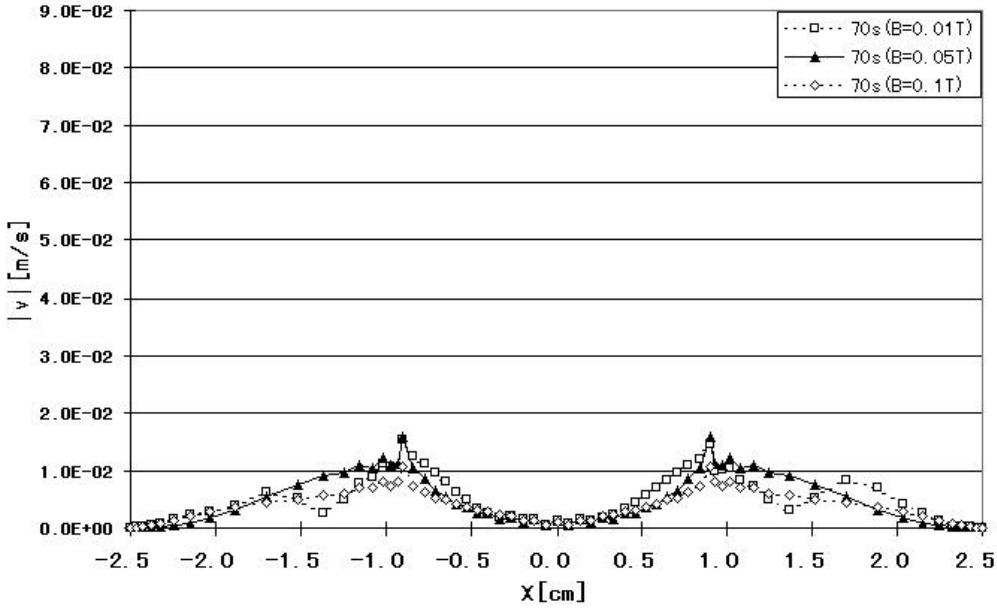
9.0E-02
8.0E-02
7.0E-02
6.0E-02
5.0E-02
4.0E-02
3.0E-02
2.0E-02
1.0E-02
0.0E+00
|v| [m/s]
-2.5 -2.0 -1.5 -1.0 -0.5 0.0 0.5 1.0 1.5 2.0 2.5
X[cm]
70s(B=0.01T)
70s(B=0.05T)
70s(B=0.1T)

(a)

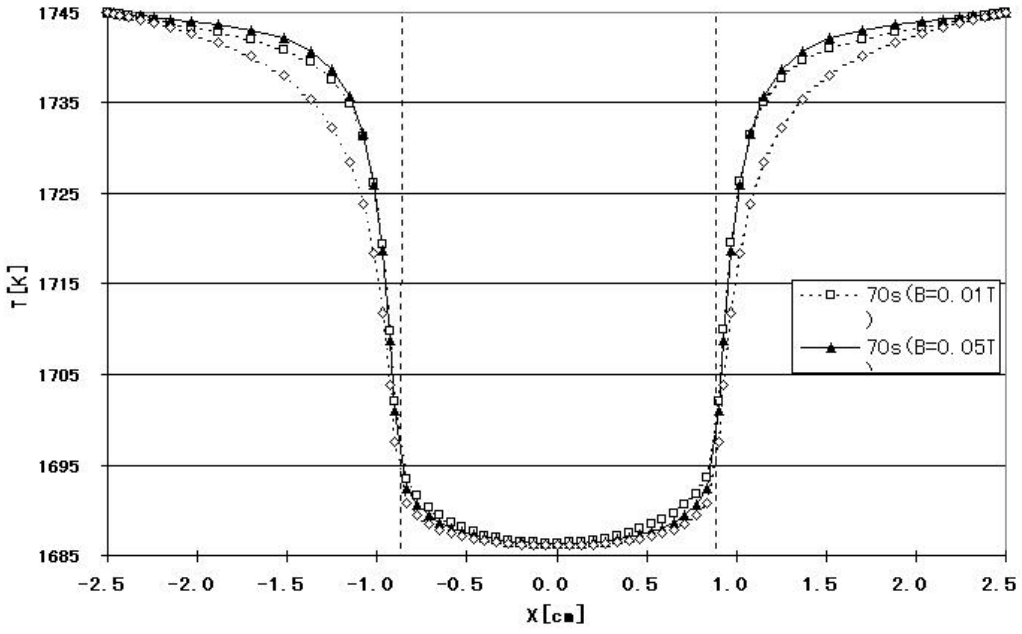
1745
1735
1725
1715
1705
1695
1685
T[K]
-2.5 -2.0 -1.5 -1.0 -0.5 0.0 0.5 1.0 1.5 2.0 2.5
X[cm]
70s(B=0.01T)
70s(B=0.05T)

(b)

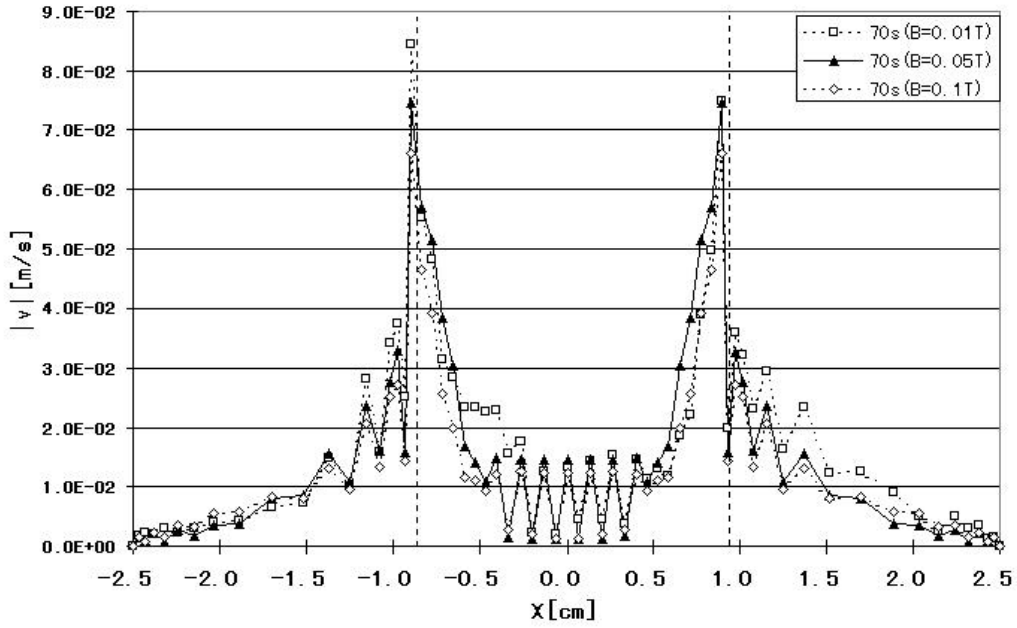

(c)

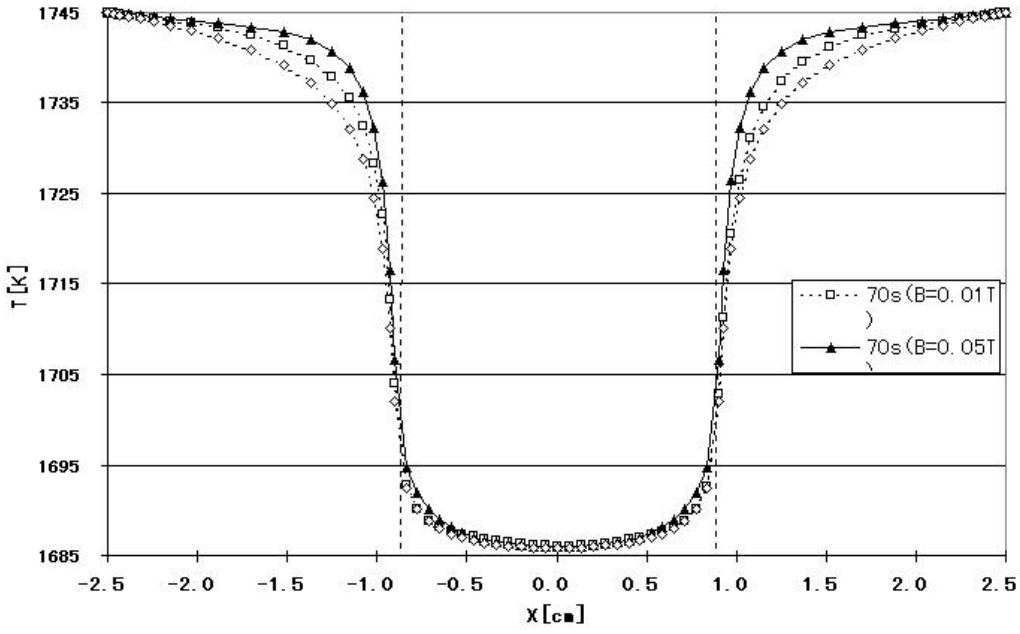

(d)

Figure 9 : Comparison of velocity and temperature distributions near the interface between a slip condition (a), (b) and Marangoni convection (c), (d) with $\sigma_T = -1.0 \times 10^{-5}$N/mK, respecitvely with the parameter B_0 at y =0.00m and $z = 2.47 \times 10^{-2}$m.

of the melt, and it restrains the intensity of the convection. On the other hand the Lorentz force does not work to the flow whose direction is parallel to the center axis. Thus the flow moves up and down mainly on the vertical plane as shown in Fig. 7 (a), (c). As a result, the flow pattern becomes restored to axisymmetry on the vertical plane (see Fig. 7 (a), (c)) and isotropy on the horizontal cut (see Fig. 7 (b), (d)) just as it does at 10s in Fig. 3 (a), (d), (g), (j).

Fig. 8 shows the comparison of the circumferential velocity distributions between a slip condition and Marangoni convection at 70s with the parameter B_0. In both conditions, the magnitude of the velocity fluctuates in B_0 = 0.01T. This means the value is not enough for cooling down the melt condition. Although the fluctuation is almost periodic on a slip condition, it becomes non-periodic by adding the Marangoni effect. On the other hand the magnitude of the velocity becomes constant in the cases of B_0 = 0.05T, 0.1T. This means the flow is well controlled by the magnetic force. However it is necessary that the melt should be fully stirred to realize the good quality products. So the case of B_0 =0.05T is superior to the one of B_0 = 0.1T in this study.

Fig. 9 shows the comparison of velocity and temperature distributions near the interface between a slip condition and Marangoni convection with the parameter B_0. On a slip condition, the velocity distributions near the interface between the single crystal and the melt are stable, and the gradient becomes smaller and smoother as B_0 increases as shown in Fig. 9 (a). However, the instability of the velocity distributions near the interface shown in Fig. 4 (a) still remains in the case considering the effect of Marangoni convection (see Fig. 9 (c)) even though the whole flow pattern keeps symmetrical structure as shown in Fig. 7 by imposing the vertical magnetic field. Although this instability is a little restrained by increasing the magnitude of B_0, the oscillation near the single crystal does not disappear. In contrast with the velocity distributions, the temperature distributions near the interface are relatively smoother and there are little differences between a slip condition and Marangoni convection. As the Lorentz force works in the opposite direction of the flow near the free surface, the convection of temperature also restrains by imposing strong magnetic field. Thus the smallest gradient of temperature is observed on both conditions when B_0 = 0.1T is imposed (see Fig. 9 (b), (d)).

8 Conclusions

3D unsteady numerical simulations of the CZ method considering the effect of Marangoni convection are carried out by means of the GSMAC-FEM. In this study the direction of the natural convection and Marangoni convection is the same near the free surface. So the flow becomes more dynamic by considering the effect of Marangoni convection than a slip condition because of the increase of Reynolds number, and the flow structure becomes asymmetrical in the early stage. In the circumferential direction, the distributions of the magnitude of both velocity and temperature show periodic motions whose wavelengths are equal to 1/8 of the circumference at 10s. Then the wavelengths double, and the distributions become finally non-periodic at 50s. As the absolute value of σ_T increases in the range of $0.0 - 1.5 \times 10^{-5}$N/mK, the instability of the melt is observed earlier. Moreover, it is found that Marangoni convection causes the oscillatory behavior of the magnitude of velocity just under the single crystal. Although the flow structure keeps symmetrical by imposing the vertical magnetic field more than B_0 = 0.05T at 70s, the instable motion still remains under the single crystal. Thus, it is confirmed that the effect of Marangoni convection is essential in the CZ process.

References:

Azami, T.; Nakamura, S.; Hibiya, T.; Mukai, K. (2000): The effect of oxygen on the Marangoni flow of molten silicon. *ISIJ International*, vol. 40, pp. S153-S156.

Frank, S.; Schwabe, D. (1997): Temporal and spatial elements of thermocapillary convection in floating zones. *Experiments in Fluids*, vol. 23, pp. 234-251.

Imaishi, N.; Yasuhiro, S.; Sato, T.; Yoda, S. (1999): Three dimensional numerical simulation of oscillatory Marangoni flow in half-zone of low Pr fluids. *SPIE*, vol. 3792, pp. 344-352.

Lee, Y. -S.; Chun, Ch. -H. (1997): Experiments on the oscillatory convection of low Prandtl number liquid in Czochralski configuration for crystal growth with cusp magnetic field. *J. Crystal Growth*, vol. 180, pp. 477-486.

Nakamura, S.; Hibiya, T.; Kakimoto, K.; Imaishi, N.; Nishizawa, S.; Hirata, A.; Mukai, K.; Yoda, S.;

Morita, T.S. (1998): Temperature fluctuations of the Marangoni flow in a liquid bridge of molten silicon under microgravity on board the TR1-A-4 rocket. *J. Crystal Growth*, vol. 186, pp. 85-94.

Schwabe, D; Scharmann, A. (1979): Some evidence for the existence and magnitude of a critical Marangoni number for the one set of oscillatory flow in crystal growth melt. *J. Crystal Growth*, vol. 46, pp. 125-131.

Sumiji, M.; Nakamura, S.; Omura, K.; Hibiya, T. (2000): Optical measurement of resonant oscillation and Marangoni convection-induced oscillation in a molten silicon surface. *Jpn. J. Appl. Phys.*, vol. 39, pp. 3688-3693.

Tanahashi, T.; Okanaga, H.; Saito, T. (1993): GSMAC finite element method for unsteady incompressible Navier-Stokes equations at high Reynolds numbers. *Inter. J. Numerical Methods in Fluids*, vol. 11, pp. 479-499.

Tanahashi, T.; Oki, Y.; Henjes, K. (1993): An application of GSMAC-FEM to electrically conducting fluid flows driven by Lorentz force. *Comp. Fluid Dyn.*, vol. 1, pp. 233-248.

Zeng, Z.; Mizuseki, H.; Higashino, K.; Kawazoe, Y. (1999): Direct numerical simulation of oscillatory Marangoni convection in cylindrical liquid bridges. *J. Crystal Growth*, vol. 204, pp. 395-404.